Available online at www.sciencedirect.com
SCIENCE DIRECT®
PERGAMON
International Journal of Heat and Mass Transfer 46 (2003) 3119–3133
International Journal of HEAT and MASS TRANSFER
www.elsevier.com/locate/ijhmt

Effect of cross-sectional aspect ratio on turbulent heat transfer in an orthogonally rotating rectangular duct with angled rib turbulators

Akira Murata *, Sadanari Mochizuki

Department of Mechanical Systems Engineering, College of Engineering, Tokyo University of Agriculture and Technology, 2-24-16 Nakacho, Koganei, Tokyo 184-8588, Japan

Received 28 June 2002

Abstract

Heat transfer in a rotating rib-roughened rectangular duct was numerically simulated by using the large eddy simulation with a Lagrangian dynamic subgrid-scale model. The rotation number and the duct cross-sectional aspect ratio (0.25, 0.5, 1.0, 2.0, and 4.0) were varied for a friction Reynolds number of 350 and rib angle of 60°. The present results clearly showed the locally high heat transfer at several locations and how it was changed by the duct aspect ratio. The dissimilarity between the streamwise velocity and temperature was observed for all the aspect ratio cases in the rotating case.

1. Introduction

In the development of high performance gas turbines, effective blade cooling is essential because the higher efficiency of the turbine requires a higher inlet gas temperature. Generally, this blade cooling is performed by film cooling at the external surface of the turbine blade and also by internal forced-convection cooling which uses winding flow passages inside the turbine blade. In internal forced-convection cooling, the real phenomena are very complicated due to external forces: the Coriolis force and the buoyancy force in the centrifugal acceleration field. In addition to these external forces, the effect induced by turbulence promoters (ribs) installed on the thermally severe opposing internal-surfaces results in phenomena that are far from understood [1].

As for the local heat transfer of a rib-roughened duct, several researchers investigated the spatial variation of the local heat transfer [2–9]. In these studies, the heat transfer variation induced by the flow separation and reattachment behind the rib was captured to a certain extent. However, it is difficult to perform the experiments in a rotating condition which can identify both the flow structure and its influence on the heat transfer at the same time. Thus, further progress in experimental studies has so far been prevented.

In previous numerical studies of rib-roughened ducts, the Reynolds-averaged Navier–Stokes equation with a turbulence model was solved for transverse [10] and angled [11,12] rib configurations. Launder et al. [13] pointed out that in order to quantitatively simulate the flow in a rotating system, the second moment closure, that is, the Reynolds stress equation model, is a minimum requirement considering a non-isotropic effect of the Coriolis force on turbulence. Although this approach using the Reynolds-averaged turbulence model could reproduce the heat transfer of blade cooling to a certain extent, even the Reynolds stress equation model has empirical constants and functions, and therefore the applicability of the model should carefully be examined. Recent advancement in computers enables us to numerically simulate the fluctuating components of the turbulent flow by using the large eddy simulation (LES)

* Corresponding author. Tel.: +81-42-388-7089; fax: +81-42-385-7204.
E-mail address: murata@mmlab.mech.tuat.ac.jp (A. Murata).

0017-9310/03/$ - see front matter © 2003 Elsevier Science Ltd. All rights reserved.
doi:10.1016/S0017-9310(03)00080-2

Nomenclature

A_R	duct cross-sectional aspect ratio ($=H/W$)
c_p	specific heat, J/(kg K)
C_S	Smagorinsky constant
D	hydraulic diameter (= rib pitch), m
e	side length of ribs, m
f	friction coefficient ($=\Delta p/(2\rho U_m^2)$)
F_i	external force term
h	heat transfer coefficient, W/(m^2 K)
H	duct height, m
j	Colburn's j factor ($=Nu_m/(Re_m Pr^{1/3})$)
ℓ	length scale ($=0.5D$), m
L_p	peripheral location
Nu	Nusselt number ($=hD/\lambda$)
P	rib pitch ($=D$), m
Δp	pressure loss in streamwise length D, Pa
Pr	Prandtl number ($=0.71$)
Pr_{SGS}	Prandtl number of subgrid-scale model ($=0.5$)
$\dot{q}$	wall heat flux, W/m^2
Re_m	Reynolds number based on bulk mean velocity ($=U_m D/\nu$)
Re_*	Reynolds number based on friction velocity ($=u_*\ell/\nu$)
Ro_m	rotation number based on bulk mean velocity ($=\omega D/U_m$)
Ro_*	rotation number based on friction velocity ($=\omega\ell/u_*$)
S_{ij}	rate-of-strain tensor
t	dimensionless time
T	temperature, K
T_b	bulk temperature, K
T_τ	friction temperature ($=\dot{q}/(\rho c_p u_*)$), K
u, v, w	dimensionless velocities in x, y, z directions
u_*	mean friction velocity, m/s
U_m	mean velocity, m/s
W	duct width, m
x, y, z	dimensionless coordinates in transverse, vertical, and streamwise directions
$\Delta x, \Delta y, \Delta z$	grid spacing in x, y, z directions
$\alpha_{SGS\,j}$	subgrid-scale energy flux
$\Delta_1, \Delta_2, \Delta_3$	grid spacing in ξ, η, ζ directions expressed in (x, y, z) coordinates' scale (in this study, $\Delta_1=\Delta x/\sin\gamma$, $\Delta_2=\Delta y$, $\Delta_3=\Delta z$)
γ	rib angle, deg
λ	thermal conductivity, W/(m K)
ν	kinematic viscosity, m^2/s
ν_{SGS}	dimensionless subgrid-scale eddy viscosity
ω	angular velocity, rad/s
ρ	density, kg/m^3
θ	dimensionless temperature ($=(T-T_b)/T_\tau$)
$\tau_{SGS\,ij}$	subgrid-scale stress tensor
τ_w	streamwise component of wall shear stress, Pa
ξ, η, ζ	curvilinear coordinates

Subscripts and superscripts

B	Blasius
L	local value
m	duct average or based on mean velocity
w	wall
∞	fully developed
$*$	friction velocity or defined by using u_*
$+$	dimensionless value based on inner scales
$-$	grid resolvable component

or the direct numerical simulation (DNS). Because LES and DNS directly resolve temporal variation of the fluctuating components, the results are more universal, in other words, more free from the empirical modeling than the Reynolds-averaged turbulence models. Although LES also has empirical constants and functions, the modeling of the turbulence is confined to the subgrid-scale turbulence, and therefore the effect of the empirical modeling on the result is ideally less than that in the Reynolds stress equation model. So far, the turbulent flow in a stationary smooth duct with a square cross section was solved using DNS [14,15] and LES [16,17]. Recently, the authors performed the numerical analyses by using a dynamic subgrid-scale model for a rotating smooth duct of which cross section was square [18] and rectangular [19], and the technique was further applied to a rotating transverse-rib-roughened duct [20,21]. In our previous numerical results, the followings were examined and clarified: the effect of duct cross-sectional aspect ratio on the Coriolis induced secondary flow, the dissimilarity between velocity and temperature fields induced by the flow separation and reattachment due to the ribs, and the very high heat transfer area located in front of the ribs which was caused by the unsteady movement of the separation bubbles there. Further investigation was performed for the angled rib effect on the heat transfer in a straight square duct using a coordinate system fitted to the angled ribs [22,23]. However, the effect of the duct cross-sectional aspect ratio on the fluid flow and heat transfer in the angled-rib-roughened duct has not been discussed yet. In the smooth duct and the transverse-rib-roughened duct of Murata and Mochizuki [19,21], the duct cross-sectional aspect ratio significantly affected the fluid flow and heat transfer through the intensity of the Coriolis induced secondary flow and the area fraction of the rib-rough-

ened surface, and therefore it can be estimated that the angled rib case is also significantly affected by the duct aspect ratio.

This study examines how the duct cross-sectional aspect ratio affects the effect of the Coriolis and angled-rib induced secondary flows on the flow and heat transfer. The LES was performed for an angled-rib-roughened rectangular duct with and without rotation. The dynamic subgrid-scale model was adopted considering the highly three-dimensional flow structure of the rib-roughened duct. The effects of the flow separation and reattachment caused by the ribs, the secondary flow induced by the angled ribs, and the Coriolis force on the heat transfer are examined by changing the duct cross-sectional aspect ratio.

2. Numerical analysis

Fig. 1 shows the computational domain and coordinate system used in this study. The duct had a rectangular cross section with a height of H and a width of W. The hydraulic diameter, D, was calculated as $2HW/(H+W)$. The coordinate system was fixed to a rotating duct which had an angular velocity of ω. The streamwise (radially outward) direction was chosen in the z direction; the x and y directions were transverse and perpendicular directions to trailing and leading walls, respectively. Ribs were installed with the in-line arrangement on the trailing and leading walls with the rib angle of γ. In this study, the buoyancy force was ignored, and the case of $\gamma = 60°$ was treated changing the duct cross-sectional aspect ratio, A_R $(= H/W)$, among the following five values: 0.25, 0.5, 1.0, 2.0, and 4.0. By assuming the periodicity of the flow field with the streamwisely repeated ribs, streamwise one span was chosen for the computational domain. The cross section of the rib was square (side length $e = 0.1D$), and the streamwise pitch, P, was set equal to the hydraulic diameter, D. This rib arrangement gave the rib height-to-hydraulic diameter ratio $e/D = 0.1$ and the rib pitch-to-rib height ratio $P/e = 10$. This rib arrangement was chosen because it was within the previously reported optimal range considering both the Nusselt number and the friction factor [24,25]. The rib angle, 60°, was chosen as the angle which gave the maximum heat transfer in Han et al. [26].

The present procedure of the numerical analysis is the same as our recent studies [22,23] which is the extension of our procedure in the Cartesian coordinate system [18–21] to the generalized curvilinear coordinate system. After applying a filtering operation to the incompressible Navier–Stokes equation with a filter width equal to the grid spacing [16], the dimensionless governing equations scaled by a length scale, ℓ $(=0.5D)$, and mean friction velocity, u_*, became a set of dimensionless governing equations with respect to grid resolvable components indicated by overbars as $(\bar{u}, \bar{v}, \bar{w})$ under the assumption of constant fluid properties. In order to simulate a fully developed situation, the pressure and temperature fields were decomposed into the steady and streamwisely linear component and the remaining component [27]. By this decomposition, the latter component of the pressure and temperature fields can be treated using a periodic boundary condition in the streamwise direction. As shown in Eq. (1), F_i is an external force term including the Coriolis force, and the buoyancy term was ignored in this study. The mean pressure gradient term (with a value of 2) was added to the external force term as follows:

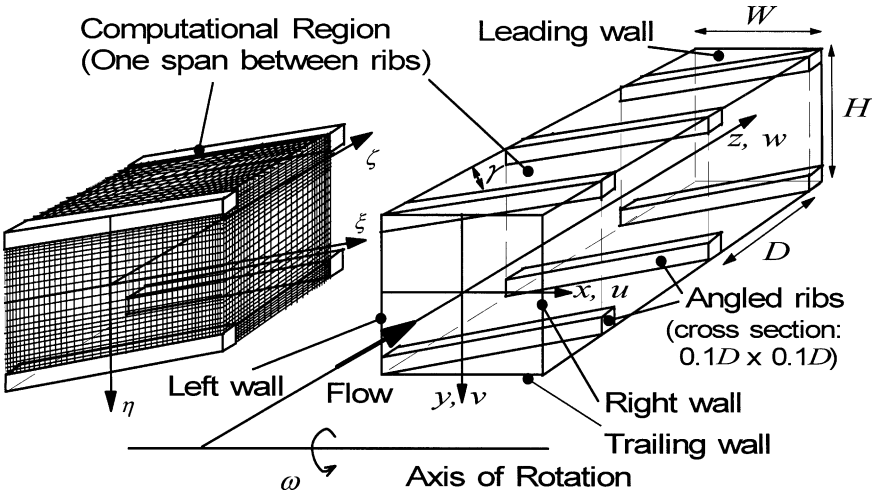

Fig. 1. Schematic of a rotating rib-roughened duct and a grid system fitted to angled ribs.

$$F_i = \begin{pmatrix} 0 \\ 2Ro_*\bar{w} \\ -2Ro_*\bar{v}+2 \end{pmatrix}. \quad (1)$$

Because the mean pressure gradient which drove the flow in the streamwise direction was set to be constant in this study, the flow rate varied depending on the flow conditions (cross-sectional aspect ratio, rib angle, and rotation number); therefore, the flow rate was not known a priori, and the flow rate was calculated from the resultant computed flow field after the fully developed condition was attained.

The temperature was made dimensionless by using a bulk temperature, T_b, and a friction temperature, T_r, as $\theta = (T - T_b)/T_r$. Accordingly, the dimensionless energy equation was derived for the grid resolvable component, $\bar{\theta}$. In order to adopt the coordinate system fitted to the angled ribs, the governing equations in the Cartesian coordinates (x, y, z) were transformed into generalized curvilinear coordinates (ξ, η, ζ) [28].

Subgrid-scale components of stress, $\tau_{SGS\,ij}$, and energy flux, $\alpha_{SGS\,j}$, are expressed as follows:

$$\tau_{SGS\,ij} = 2\nu_{SGS}\overline{S}_{ij}, \quad (2)$$

$$\alpha_{SGS\,j} = \frac{\nu_{SGS}}{Pr_{SGS}}\frac{\partial\xi^k}{\partial x_j}\frac{\partial\bar{\theta}}{\partial\xi^k}, \quad (3)$$

where,

$$\overline{S}_{ij} = \frac{1}{2}\left(\frac{\partial\xi^k}{\partial x_j}\frac{\partial\bar{u}_i}{\partial\xi^k} + \frac{\partial\xi^k}{\partial x_i}\frac{\partial\bar{u}_j}{\partial\xi^k}\right), \quad (4)$$

$$\nu_{SGS} = C_S^2(\Delta_1\Delta_2\Delta_3)^{2/3}\sqrt{2\overline{S}_{ij}\overline{S}_{ij}}. \quad (5)$$

In our previous studies for the transverse 90° rib cases [20,21], the dynamic subgrid-scale model developed by Germano et al. [29] was used in order to calculate the value of C_S as a function of spatial location with the stable computational procedure of Lilly [30]; C_S was averaged taking advantage of the symmetric property in the transverse direction in addition to the time averaging in order to exclude negative values of C_S. However, the angled rib case of this study has no geometric symmetry in the transverse direction, and therefore we adopted the Lagrangian dynamic subgrid-scale model of Meneveau et al. [31] which averages the value of C_S along the path-line for a certain distance. As for the coefficient of the Lagrangian averaging time scale, the same value of 1.5 as that in [31] was used. The turbulent Prandtl number for the subgrid-scale component, Pr_{SGS}, was set to 0.5 [32]. The width of the test filter was double the grid spacing.

Discretization was performed by a finite difference method using the collocated grid system [28]. The spatial and temporal discretization schemes were similar to those of Gavrilakis [15]: the second order central differencing method and the Crank–Nicolson method for the viscous term, and the second order differencing method satisfying the conservative property and the second order Adams–Bashforth method for the convective term. The external force term was also treated by the second order Adams–Bashforth method. The pressure field was treated following the MAC method [33], and the algebraic equation for each variable was solved by using the SOR method. The computational domain was one span between streamwise consecutive ribs (see Fig. 1), and its dimensions were $2\times2\times2$, $1.5\times3\times2$, and $1.25\times5\times2$ in x, y, z directions for $A_R = 1.0$, 2.0, and 4.0, respectively. It can be expressed by using an inner length scale, ν/u_*, as $700\times700\times700$ for $A_R = 1.0$.

As a basic condition (Case A), the Reynolds number, $Re_*(= u_*\ell/\nu)$, was 350, and the rotation number, $Ro_*(= \omega\ell/u_*)$, was 0 and 1.0. The higher Ro_* of 2.0 and 5.0 was computed only for $A_R = 1.0$. The conversion of the dimensionless numbers of this study (Re_*, Ro_*) defined by the mean friction velocity and the length scale, $0.5D$, into those of (Re_m, Ro_m) defined by the mean velocity and the hydraulic diameter, D, was summarized in Table 1. As explained above, the value of Re_m varies depending on the flow condition in Case A. In order to extract only the duct aspect ratio effect on the heat transfer, additional computations of Case B were performed keeping the values of Re_m and Ro_m identical to those of $A_R = 1.0$ ($Re_m \fallingdotseq 3000$ and $Ro_m \fallingdotseq 0.4$) by adjusting the Reynolds and rotation numbers, Re_* and Ro_*. The adjusted values of Re_* and Ro_* were determined by using the results of Case A; assuming the normalized friction factor to be unchanged within this adjustment range, the necessary adjustment on Re_* and Ro_* can be calculated. The condition of Case B is also summarized in Table 1.

At the wall boundary, no-slip and constant heat flux conditions were imposed, although the rib side surfaces were set to be adiabatic. The adiabatic condition at the rib side surfaces was adopted to preserve the linear increase of the bulk temperature and also to consider the previous experiments in which the ribs were not heated. An additional computation with the constant heat flux condition at the rib side surfaces was also performed, and it was found that even when the rib side surfaces were heated, the conclusions of this study were not changed. At the inlet and outlet boundaries, the periodic boundary condition [27] was imposed in order to obtain a fully developed flow. The validity of the one-span computational domain with the streamwise periodic boundary condition was examined by computing the streamwise one- and three-span cases with the same round-type ribs as used in Stephens et al. [11] and Banhoff et al. [12], and as shown in Table 2, no major difference was observed between one- and three-span results. The boundary conditions of the intermediate velocities and the pressure were set following the procedure of [34,35].

Table 1
Dimensionless number range (Re_*, Ro_*) of this study and its conversion into the conventional form (Re_m, Ro_m) (The data of 90° rib are from Murata and Mochizuki [21])

	A_R	0.25	0.5	1.0	2.0	4.0
	γ	60°	60°	60° (90°)	60° (90°)	60° (90°)
Case A ($Re_* = 350$)						
$Ro_* = 0$ ($Ro_m = 0$)	Re_m	2705	2763	3148 (4106)	4199 (5766)	7434 (9231)
$Ro_* = 1$	Re_m	2792	3008	3645 (3959)	4822 (5264)	6943 (7215)
	Ro_m	0.501	0.465	0.384 (0.354)	0.290 (0.266)	0.206 (0.194)
$Ro_* = 2$	Re_m	–	–	3858	–	–
	Ro_m	–	–	0.726	–	–
$Ro_* = 5$	Re_m	–	–	4650	–	–
	Ro_m	–	–	1.505	–	–
Case B ($Re_m \fallingdotseq 3000$)						
$Ro_m = 0$ ($Ro_* = 0$)	Re_*	399.7	–	350	–	165.0
	Re_m	2986	–	3148	–	3309
$Ro_m \fallingdotseq 0.4$	Re_*	388.8	–	307.8	–	177.2
	Re_m	2929	–	3148	–	2768
	Ro_*	0.756	–	1	–	1.660
	Ro_m	0.401	–	0.391	–	0.425

Table 2
Effect of periodic boundary condition in streamwise direction on friction factor, f/f_B, and wall-averaged Nusselt number, Nu_w/Nu_∞ (60° rib, $A_R = 1.0$, $Re_* = 350$, $Ro_* = 0$, $e/D = 0.1$, and $P/e = 10$)

	Re_m	f/f_B	Nu_w/Nu_∞		
			Ribbed wall	Left wall	Right wall
With square ribs (one-span, 400,000 steps)	3148	9.38	3.43	2.80	2.96
With round-type ribs (one-span, 200,000 steps)	3176	9.23	3.22	2.58	2.75
With round-type ribs (three-span, 200,000 steps)	3157	9.33	3.33	2.51	2.79

The grids in the physical domain were contracted to both the walls and the rib surfaces by using a tangent hyperbolic function (see Fig. 1). The grid number was mainly $47 \times 47 \times 47$, and this grid configuration gave a grid spacing of $\Delta x^+ = 1.0$–38, $\Delta y^+ = 0.6$–52, and $\Delta z^+ = 4.0$–28 for $A_R = 1.0$. The effect of the grid spacing on the computed result was checked by increasing the grid number to $71 \times 71 \times 71$ for several cases. Since only for the stationary condition of $A_R = 4.0$ the quantitative difference was observed in the profiles of the streamwise velocity and temperature, for $A_R = 4.0$ the grid resolution of $71 \times 71 \times 71$ was used. The effect of the grid resolution will be further discussed in the next section. The time step interval was $\Delta t = 1.0 \times 10^{-4}$, which can be expressed as $\Delta t^+ = 0.035$ when made dimensionless by an inner time scale, v/u_*^2 for $Re_* = 350$. The computation was started using the result of the similar condition as an initial condition. The calculations were carried out to 160,000 steps to fully develop the flow in each case. After the initial 160,000 steps were performed, additional 80,000 steps ($t = 8$ or $t^+ = 2800$) were performed for computing the statistical values. The 80,000 step computation needed about 15CPU hours using NEC SX4B. As for the case of $A_R = 1.0$, the previous data [22] of 400,000 steps were used. In this study, the total time step was decreased to 80,000 steps, and the wide range of A_R was investigated. This reduction in the total time step did not change the wall-averaged Nusselt number, although the symmetry of the flow and heat transfer fields demanded by the geometrical symmetry deteriorated a little as discussed in [21] and also as will be seen in Figs. 2–4 and 8 for the stationary condition.

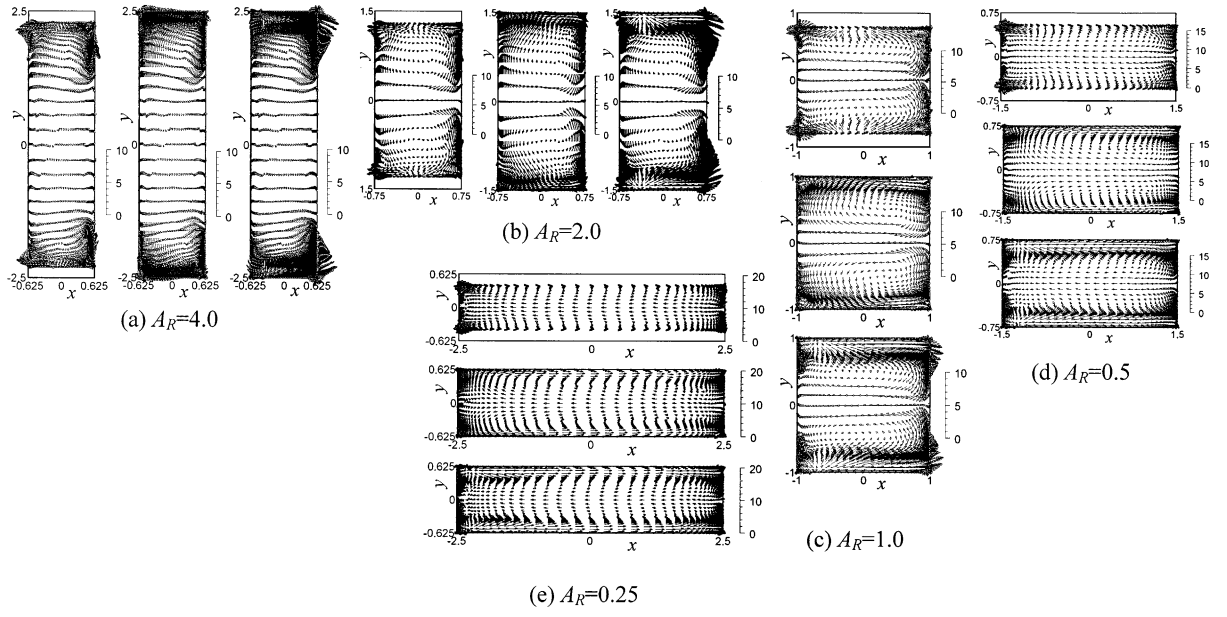

Fig. 2. Change in time-averaged velocity vectors of secondary flow in ξ–η plane at three different streamwise locations (Case A, 60° rib, and $Ro_* = 0$; figures are projected onto x–y plane. Left, middle, and right (or top, middle, and bottom) figures are in the plane at rib location, at midpoint between ribs, and in front of ribs (a half of rib width from ribs), respectively).

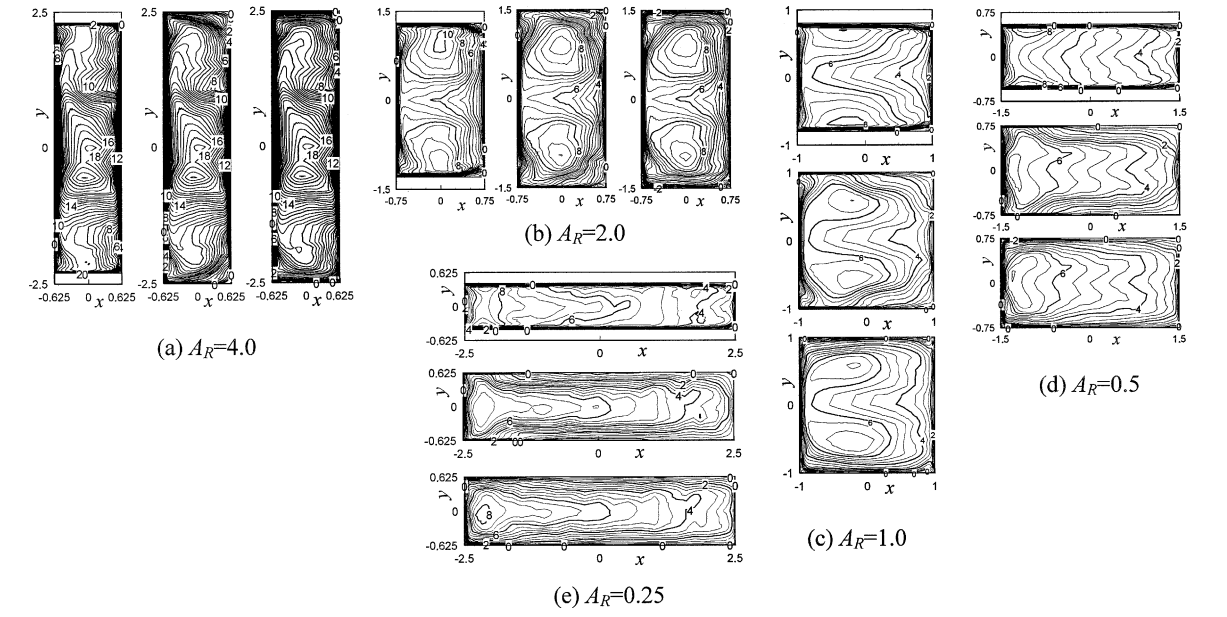

Fig. 3. Change in isocontours of time-averaged streamwise velocity in ξ–η plane at three different streamwise locations (Case A, 60° rib, and $Ro_* = 0$; legend is the same as that of Fig. 2).

3. Results and discussion

Fig. 2 shows the time-averaged velocity vectors $(\bar{u}, \bar{v})$ for the stationary condition of Case A in the ξ–η plane which is parallel to the 60° ribs. In the figure, the value in the ξ–η plane is projected onto the x–y plane, and the values at three different streamwise locations are shown: from left to right (or from top to bottom) for each A_R,

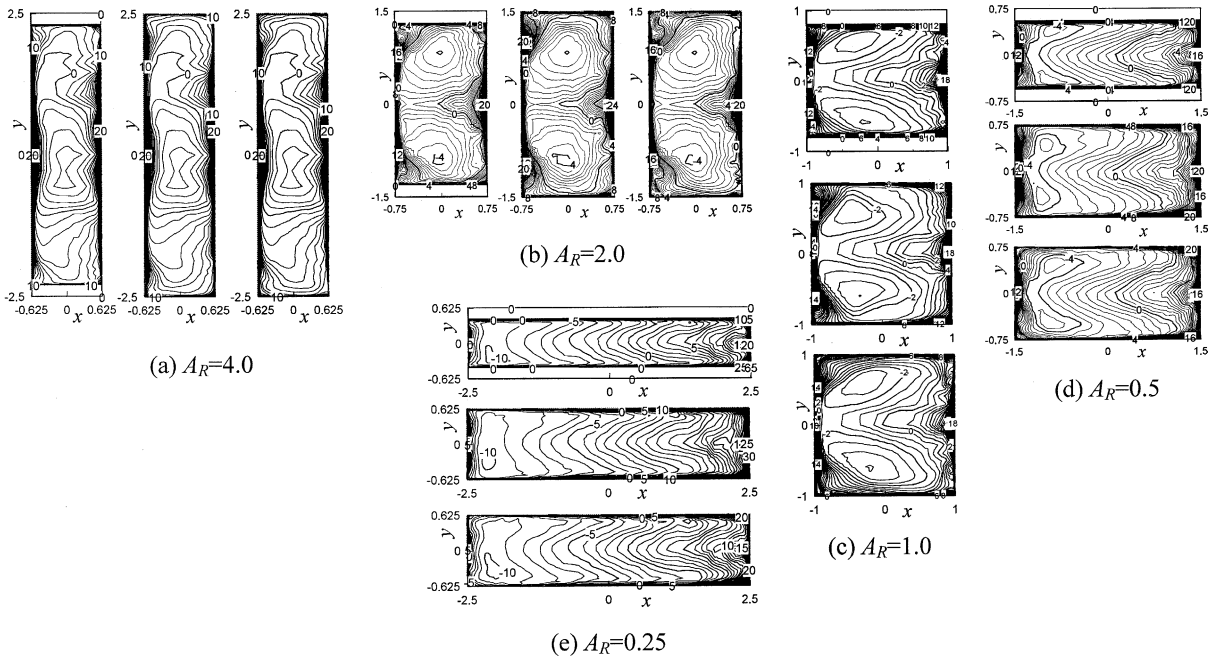

Fig. 4. Change in isocontours of time-averaged temperature in ξ–η plane at three different streamwise locations (Case A, 60° rib, and $Ro_* = 0$; legend is the same as that of Fig. 2).

the locations are at rib location (rib streamwise center), at the midpoint between the consecutive ribs, and in front of the ribs (a half of rib width from the ribs), respectively. In the stationary condition, near the upper and lower walls of Fig. 2, the flow passing along the angled rib (from left to right in the figure) is seen; on the other hand, at about the vertical center ($y = 0$) the flow from right to left in the figure is formed as a return flow. These flows compose a pair of vortex, and it dominates the flow field in all aspect ratio cases.

Figs. 3 and 4 show the isocontours of the time-averaged streamwise velocity, $\bar{w}$, and temperature, $\bar{\theta}$, respectively, in the stationary condition of Case A. For the aspect ratio of $A_R \geqq 1.0$ (Fig. 3(a)–(c) and Fig. 4(a)–(c)), $\bar{w}$ and $\bar{\theta}$ show almost similar profiles to each other in each cross section. However, for $A_R < 1.0$ (Fig. 3(d), (e) and Fig. 4(d), (e)), the similarity between $\bar{w}$ and $\bar{\theta}$ is not preserved. The two vertically separated peaks are induced by the angled-rib induced secondary flow in most of the cases except $\bar{w}$ for $A_R = 0.5$ (Fig. 3(d)) and $\bar{w}$ and $\bar{\theta}$ for $A_R = 4.0$ and 0.25 (Figs. 3(a), (e) and 4(a), (e)). Except the case of $A_R = 4.0$, at about the vertical center ($y = 0$) of the right wall (right-hand side wall in the figure), the isocontour lines of $\bar{w}$ and $\bar{\theta}$ are projected to the duct center due to the secondary flow seen in Fig. 2, although for $A_R < 1.0$ the isocontour lines of $\bar{w}$ in the same area are not projected to the duct center as much as that of $\bar{\theta}$. As compared to the other cases, $\bar{w}$ for $A_R = 0.25$ in Fig. 3(e) gives the transversely uniform profile due to the small height of the duct.

In the rotating case ($Ro_* = 1$, Case A) of Fig. 5, for $0.5 \leqq A_R \leqq 2.0$ (Fig. 5(b)–(d)), the secondary flows induced by the angled rib and the Coriolis force interact to each other, and it results in an inclined vortex pair which induces a flow directing from the lower-right to the upper-left in the figure. This vortex pair induces the flow directing from left to right near the trailing wall (upper wall in the figure), and then the flow goes from the trailing wall to the leading wall near the right wall. In front of the rib on the leading wall, the flows induced by the angled rib (from left to right in the figure) and the Coriolis force (from right to left in the figure) collide to each other. In the vicinity of the left wall, the flow passing from top to bottom is seen. For $A_R = 4.0$ of Fig. 5(a), the flow passing from the lower-right to the upper-left becomes very weak; on the other hand, for $A_R = 0.25$ of Fig. 5(e), this secondary flow is localized near the right wall.

The vortex pair seen in Fig. 5 forms inclined profiles both in $\bar{w}$ and $\bar{\theta}$ as seen in Figs. 6 and 7, and the similarity between $\bar{w}$ and $\bar{\theta}$ breaks at all streamwise locations. Except $A_R = 0.25$, the peak of $\bar{\theta}$ (Fig. 7) at the rib location is shifted to the corner of the trailing (pressure side) and right walls; on the contrary, the peaks of $\bar{w}$ (Fig. 6) are separated into two which locate shifted to the corners of the leading (suction side) and right walls

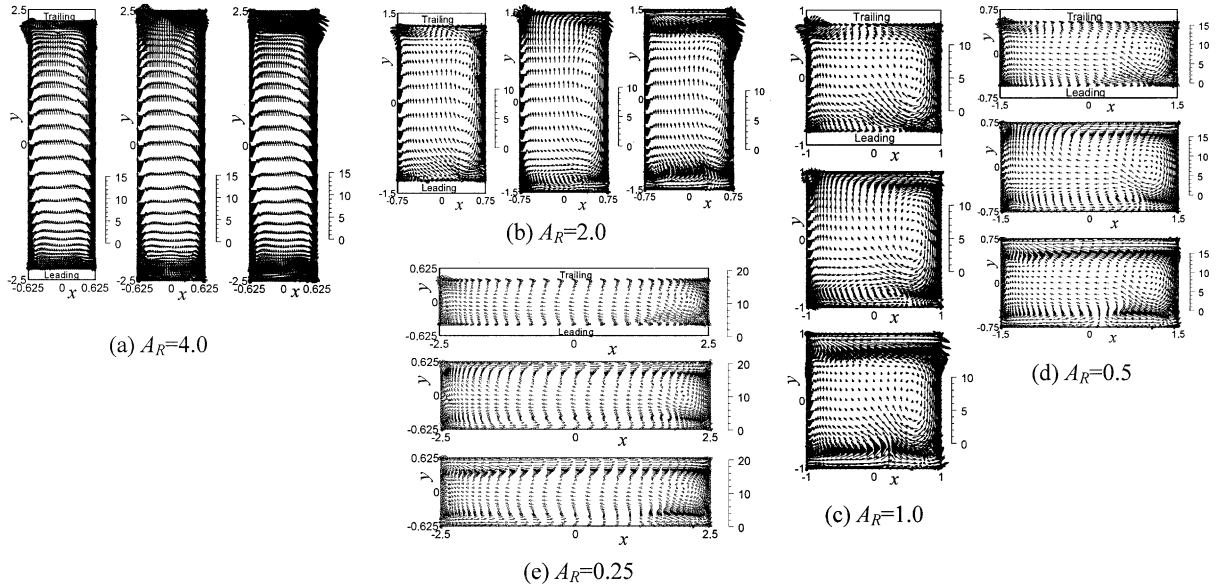

Fig. 5. Change in time-averaged velocity vectors of secondary flow in ξ–η plane at three different streamwise locations (Case A, 60° rib, and $Ro_* = 1$; legend is the same as that of Fig. 2).

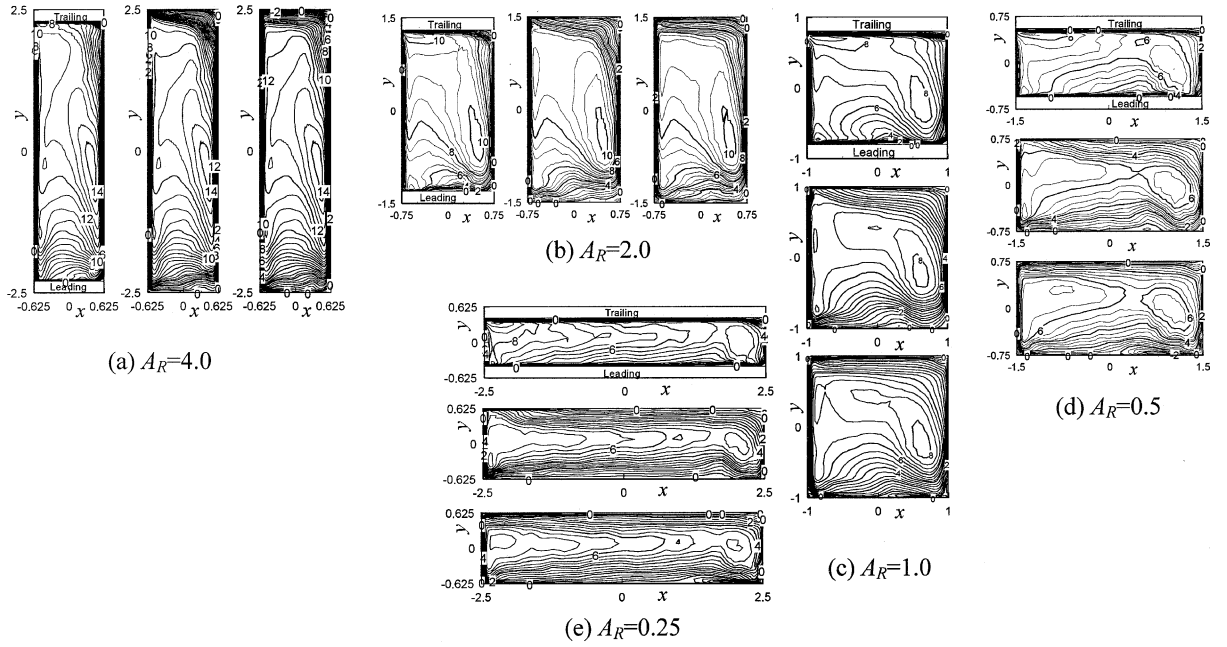

Fig. 6. Change in isocontours of time-averaged streamwise velocity in ξ–η plane at three different streamwise locations (Case A, 60° rib, and $Ro_* = 1$; legend is the same as that of Fig. 2).

and the trailing and left walls; in addition, the other weak peak can be seen at the leading-left corner in Fig. 6(b)–(d). At the other steamwise locations for $A_R \geqq 1.0$, only the peak of $\bar{w}$ near the leading-right corner remains. Generally, the larger streamwise velocity distribution in the transverse direction (the case of larger A_R) forms the more intense Coriolis induced secondary flow; on the other hand, the larger transverse width of the rib-roughened wall (the case of smaller A_R) results in the more intense angled-rib induced secondary flow.

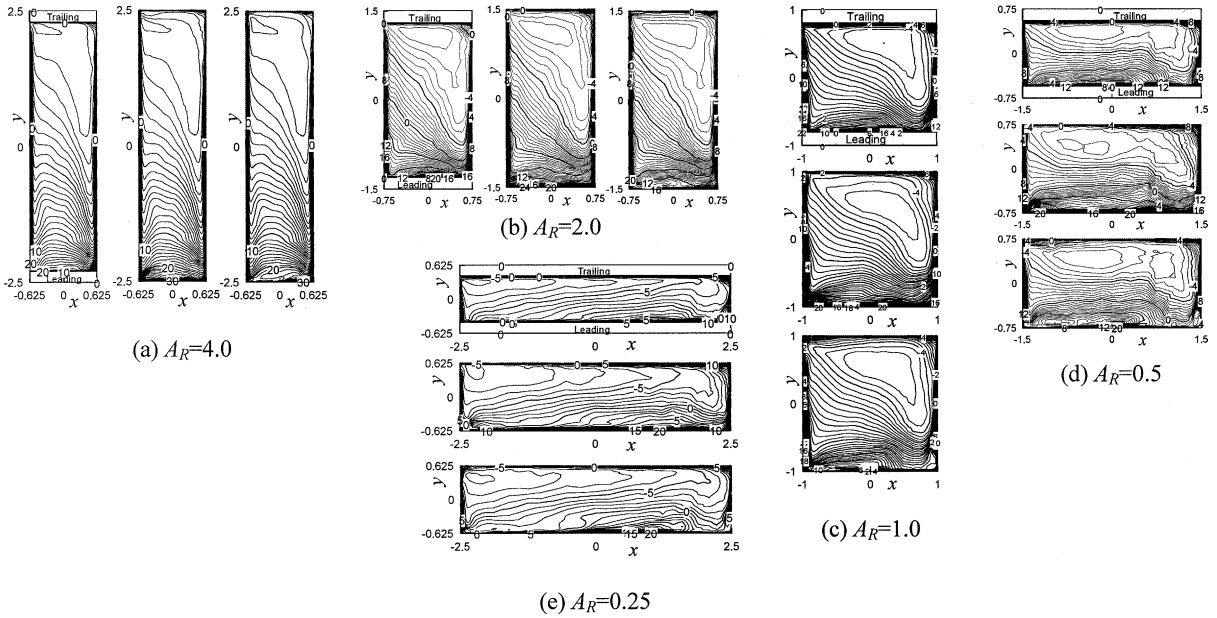

Fig. 7. Change in isocontours of time-averaged temperature in ξ–η plane at three different streamwise locations (Case A, 60° rib, and $Ro_* = 1$; legend is the same as that of Fig. 2).

Therefore, it can be said that, for the larger and smaller values of A_R, the secondary flows induced by the Coriolis force and the angled ribs become dominant, respectively. Moreover, when A_R becomes very small ($A_R = 0.25$ in Fig. 6(e)), the velocity profile becomes uniform in the transverse direction, and, at the same time, the effect of the rotation becomes small judging from the similar profile to the stationary case of Fig. 3(e). In $A_R = 0.25$, the peaks of $\bar{w}$ and $\bar{\theta}$ are shifted to the left wall both in the stationary and rotating conditions, although, in the other A_R cases, the peaks are shifted to the opposite side (the right wall) due to the rotation.

Fig. 8 shows the streamwise component of the wall shear stress (left figures) and the local Nusselt number (right figures) on the four walls for the stationary 60° rib cases (Case A). The Nusselt number was normalized using the following empirical correlation for a fully developed pipe flow [36]:

$$Nu_\infty = 0.022 Re_m^{0.8} Pr^{0.5}. \quad (6)$$

In the figures, out-of-range values are shown by white and black solid areas for very low and very high values, respectively. Zero shear stress areas are also indicated by solid white. For easier understanding of the figures, the sign of the wall shear stress ((+), (−)) and the level of the Nusselt number (high, low) are added to the figures of $A_R = 1.0$. It should be noted that the notches around the ribs are caused by the inadequate interpolation ability of the software used in drawing the figure, and the numerical results themselves do not oscillate. In Fig. 8(c) of $A_R = 1.0$, the high heat transfer area at the midpoint between the ribs is correlated with the positive wall shear stress, and the angled-rib induced secondary flow shifts the area to the left wall. On the other hand, in front of the ribs, the high heat transfer area is correlated with the negative wall shear stress. On the smooth side walls, the high heat transfer area is seen around the ribs both on the right and left walls, although at the central area the heat transfer becomes high and low on the left and right walls, respectively, due to the angled-rib induced secondary flow. How the above-mentioned characteristics for $A_R = 1.0$ are varied by the value of A_R is explained below. For $A_R > 1$ of Fig. 8(a) and (b), the high heat transfer areas at the midpoint between the ribs and in front of the ribs stay at about the transverse center because of the small width of the rib-roughened wall. At the same time, this short rib width makes the intensity of the angled-rib induced secondary flow lower, and the heat transfer becomes lower as compared to the cases of $A_R \leqq 1$. For $A_R < 1$ of Fig. 8(d) and (e), the high heat transfer areas at the midpoint between the ribs and in front of the ribs are highly shifted to the left wall and localized there. In the wall shear stress distribution near the left wall on the rib-roughened wall, a large spatial variation between the positive and negative values is observed. On the other hand, near the right wall on the rib-roughened wall, the spatial variation becomes smaller and the wall shear stress becomes almost zero. In Fig. 3(d) and (e), the region near the right wall has the

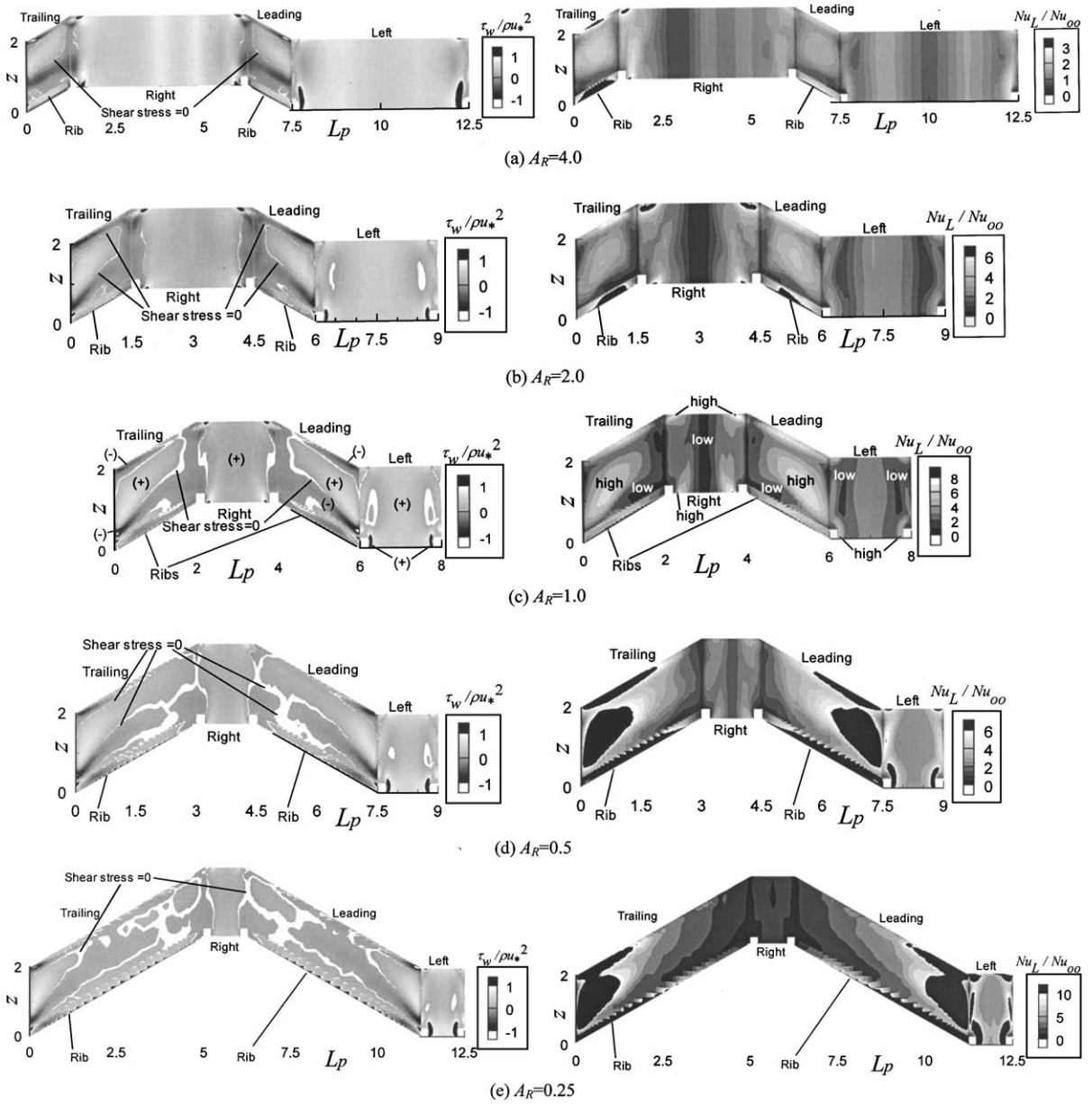

Fig. 8. Spatial variation of time-averaged streamwise wall shear stress (left) and Nusselt number (right) on four walls for 60° rib and $Ro_* = 0$ (Case A).

lower streamwise velocity, and therefore it can be said that the angled-rib induced velocity field cannot transport the sufficient momentum to the region near the right wall.

The results of the rotating case ($Ro_* = 1$, Case A) are shown in Fig. 9. On the trailing wall (pressure surface), the distribution of the rotating case is similar to that of the stationary case (Fig. 8). On the other hand, on the leading wall (suction surface), the spatial variation of the wall shear stress becomes smaller, and the Nusselt number also becomes smaller. The present results are similar to those of the smooth duct and the 90° rib-roughened duct [18–21], in which, due to the Coriolis induced secondary flow, the values of both the wall shear stress and the Nusselt number became larger and smaller on the trailing and leading walls, respectively, as compared to the stationary case; on the smooth side walls, the Nusselt number increased from the leading

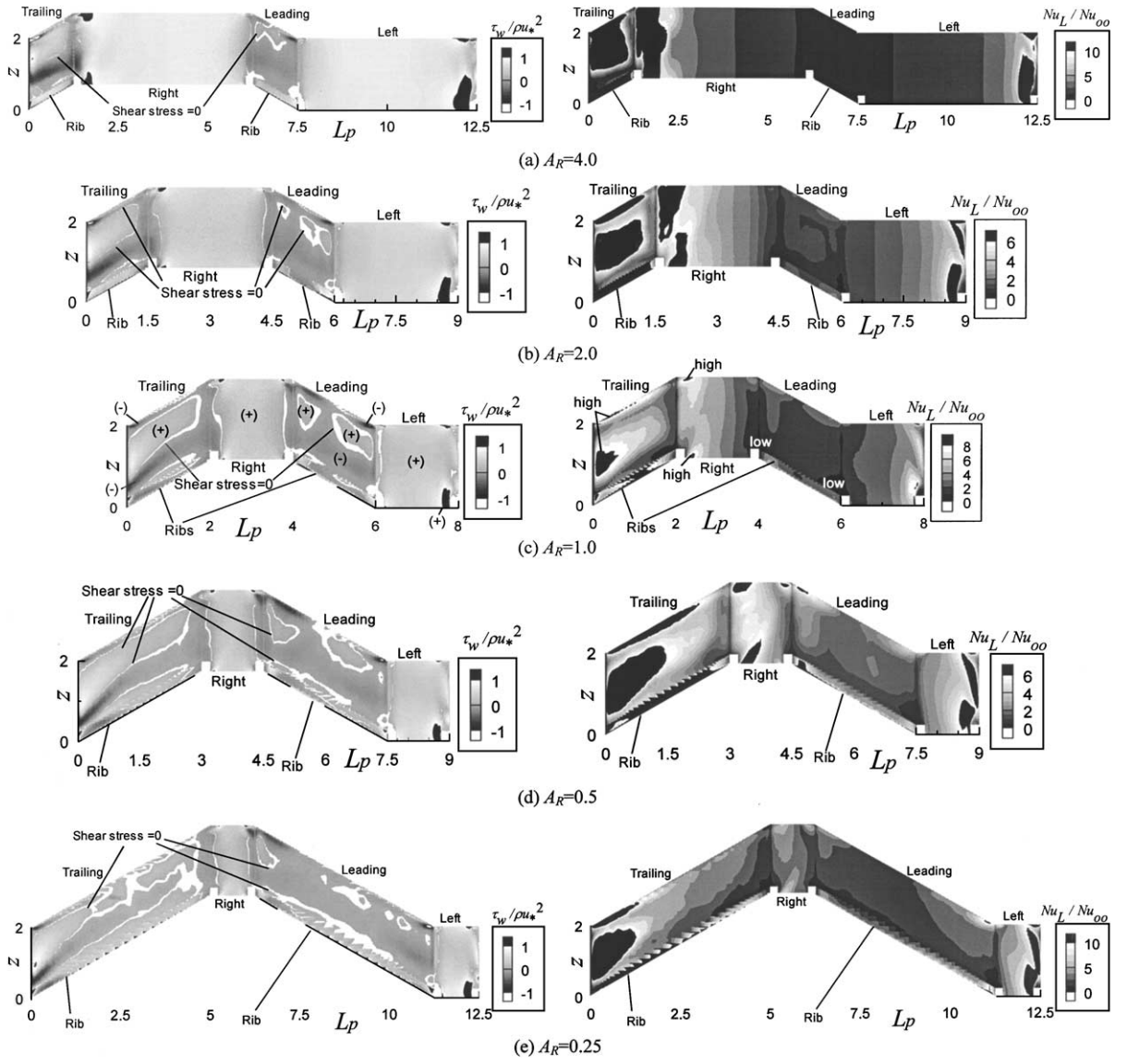

Fig. 9. Spatial variation of time-averaged streamwise wall shear stress (left) and Nusselt number (right) on four walls for 60° rib and $Ro_* = 1$ (Case A).

side to the trailing side. As explained above, when A_R is larger, the effect of the Coriolis force is larger, and the difference between the values on the trailing and leading walls becomes larger.

Here, the present numerical results are verified by comparing those with the experimental results. As examined in [22], the present numerical results gave the satisfactory agreement with the experimental results of Chandra et al. [5] (60° rib, $A_R = 1.0$, and the stationary condition) both in the local and wall-averaged Nusselt numbers. In the examination, the rib configuration was set identical to that of the experiments ($e/D = 0.063$ and $P/e = 10$). In order to evaluate the Reynolds number effect, Re_m was increased from 4398 to 8429 ($Re_* =$ 350–718), and it was confirmed that the numerical results approached to the experimental results of $Re_m =$ 30,000. The experimental and numerical wall-averaged Nusselt numbers were $Nu_w/Nu_\infty = 3.3$ and 2.9 for the rib-roughened wall, and 2.2 and 2.1 for the smooth side walls (by accident, the left- and right-wall values were same for the stationary square duct with 60° ribs).

Fig. 10 shows the dependency of the wall-averaged Nusselt number, Nu_w, and the friction factor, f, on the aspect ratio, A_R. The Nusselt number and the friction

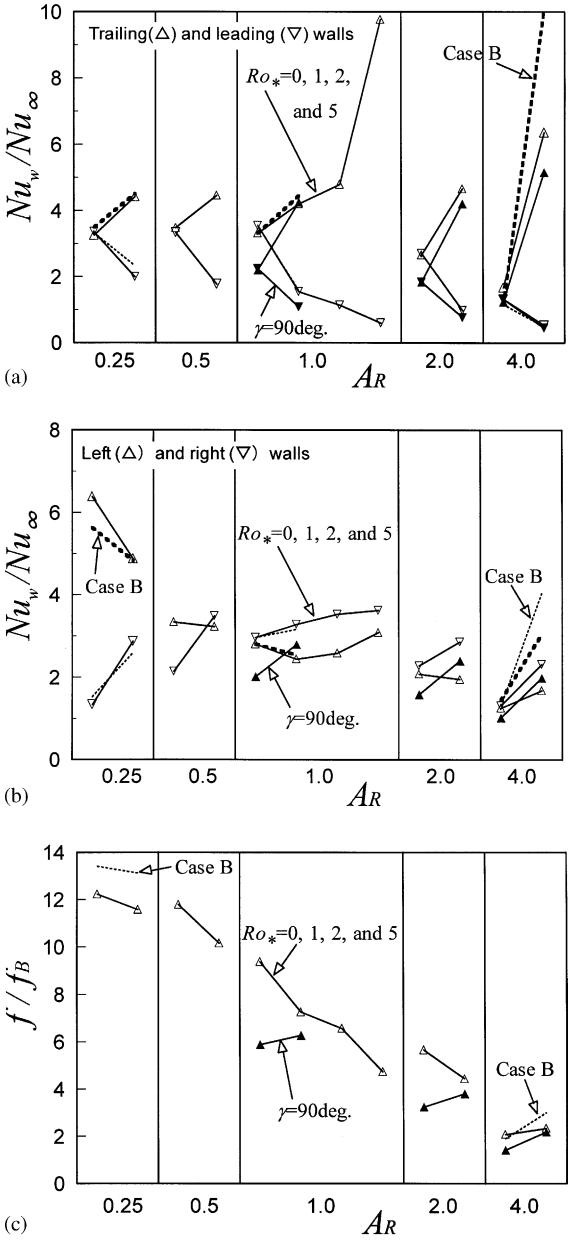

Fig. 10. Effect of duct aspect ratio and rotation on wall-averaged Nusselt number, Nu_w, and friction factor, f; open and filled symbols (Case A) are for 60° and 90° rib cases, respectively; for $A_R = 1.0$, symbols from left to right correspond to $Ro_* = 0$, 1, 2, and 5, respectively; for the other A_R cases, left- and right-hand side symbols are for $Ro_* = 0$ and 1, respectively; Case B results are shown by dotted lines, and thicker dotted lines in (a) and (b) correspond to trailing and left wall values, respectively.

factor are normalized by using Nu_∞ in Eq. (6) and f_B in the following Blasius equation:

$$f_B = 0.079 Re_m^{-0.25}. \quad (7)$$

In the figure, the left and right plots for each A_R except $A_R = 1.0$ are for the stationary and rotating ($Ro_* = 1.0$) conditions, respectively. For $A_R = 1.0$, the rotation number was varied among $Ro_* = 0$, 1, 2, and 5 corresponding to the symbols from left to right in the figure. In the figure, the adjusted Re_* and Ro_* case (Case B) is also shown with dotted lines for $A_R = 0.25$, 1.0, and 4.0.

In Fig. 10(a), the effect of the rotation increases and decreases the wall-averaged Nusselt number on the trailing and leading walls, respectively, and this tendency is common in the whole range of A_R. As compared to the 90° rib results (filled symbols) of [21], the 60° rib results (open symbols) give the higher values in the stationary condition. For $A_R \geqq 1.0$, the difference between the leading and trailing wall values of the rotating case ($Ro_* = 1$) becomes larger for the larger A_R. For $A_R = 1.0$, the result of $Ro_* = 5.0$ gives the abrupt increase on the trailing wall. For $A_R = 4.0$ the result of Case B gives the larger increase induced by the rotation on the trailing wall than that of Case A, while the other results of Case B are almost identical to those of Case A. On the smooth side walls of Fig. 10(b), the stationary results (left plot for each A_R) show a monotonic decrease for the increase of A_R on the left wall; on the other hand, on the right wall, a local maximum exists at $A_R = 1.0$. For $A_R < 1.0$, due to the angled-rib induced secondary flow in the stationary condition, the heat transfer on the left wall becomes higher than that on the right wall (see Fig. 8(d) and (e)); for $A_R \geqq 1.0$, the right and left walls have almost the same values. When the duct rotates, the difference between the left and right wall values becomes smaller for $A_R < 1.0$, and the heat transfer on the right wall becomes higher than that on the left wall for $A_R \geqq 1.0$. This tendency is also seen in Case B. The 90° rib result (filled symbols) on the side wall increases with the rotation ($Ro_* = 1$); on the other hand, the 60° rib result increases on the right wall, and on the left wall it decreases except for $A_R = 4.0$. Generally, due to the effect of the angled rib, the peaks of $\bar{w}$ and $\bar{\theta}$ are shifted to the left wall side (Figs. 3 and 4), and the heat transfer becomes higher near the left wall (Fig. 8); however, the effect of the rotation shifts the peaks to the right wall side (Figs. 6 and 7), and therefore the heat transfer near the leading wall side on the left wall becomes lower (Fig. 9). In the case of $A_R = 4.0$, the effect of the Coriolis force becomes the largest among the present A_R values, and therefore the heat transfer seems to be enhanced even on the left wall. The left wall values of $A_R = 1.0$ also show the increase for the higher rotation numbers of $Ro_* = 2$ and 5. In Fig. 10(c), the friction factors, f, of both the 60° and 90° rib cases decrease with the increase of A_R in the stationary condition, although the effect of the rotation emerges in an opposing way for $A_R \leqq 2.0$: it decreases and increases the friction factors of the 60° and 90° rib cases, respectively. The 60° rib case of $A_R = 4.0$

shows the increase in f by the rotation because of the largest Coriolis effect among the duct aspect ratios examined.

Fig. 11 shows the duct-averaged results in the friction factor, f, and the Colburn's j factor. The 90° rib results of [21] (filled symbols) are also shown in the figure. The same data are also summarized in Table 3. In the table, the results with the higher grid resolution of $71 \times 71 \times 71$ are shown with an asterisk, and it can be seen that the dependency of the results on the grid resolution is small. Because the area fraction of the rib-roughened surface becomes smaller with the increase of A_R, f and j factors become the smallest at $A_R = 4.0$. However, as explained above, the larger aspect ratio case is more affected by the rotation, and therefore, in the 90° rib case, the increase caused by the rotation becomes larger for larger A_R (see Table 3). On the other hand, in the 60° rib case, only the result of $A_R = 4.0$ is increased by the rotation, and the other cases are decreased by the rotation. This different tendency between the 90° and 60° rib cases can be explained as follows: the angled-rib induced secondary flow increases the friction and heat transfer in the stationary condition vary intensively, and the increase due to the flow field in the rotating condition cannot exceed that in the stationary condition; in other words, the flow field resulting from the interaction between the secondary flows induced by the angled ribs and the Coriolis force is not effective in the heat transfer enhancement as much as that induced alone by the angled ribs in the stationary condition.

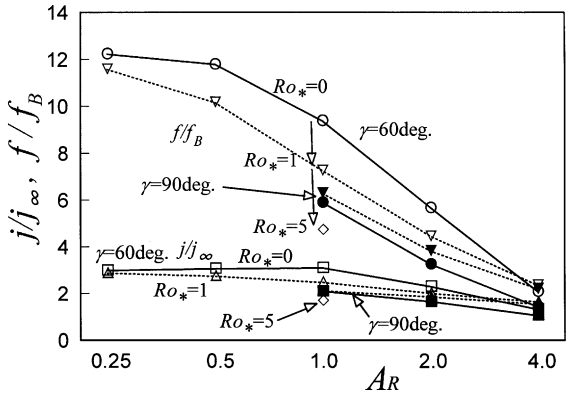

Fig. 11. Effect of rotation and cross-sectional aspect ratio on f and j factors (Case A: filled and open symbols are for 90° and 60° rib cases, respectively; ○●: f/f_B for $Ro_* = 0$, ▽▼: f/f_B for $Ro_* = 1$, □■: j/j_∞ for $Ro_* = 0$, △▲: j/j_∞ for $Ro_* = 1$, ◇: for $Ro_* = 5$).

Table 3
Enhancement factors in f and j caused by rotation and aspect ratio (90° rib data are from Murata and Mochizuki [21] and shown in parentheses. The values with an asterisk are for higher grid resolution of $71 \times 71 \times 71$)

	A_R	0.25	0.5	1.0	2.0	4.0
	γ	60°	60°	60° (90°)	60° (90°)	60° (90°)
Case A ($Re_* = 350$)						
$Ro_* = 0$	f/f_B	12.23	11.78	9.38	5.66	
		12.26*		8.86*	5.47*	2.08*
				(5.89)	(3.25)	(1.43)
	j/j_∞	2.98	3.06	3.09	2.30	
		3.15*		3.01*	2.36*	1.31*
				(2.09)	(1.65)	(1.06)
$Ro_* = 1$	f/f_B	11.57	10.16	7.25	4.45	
		12.13*		7.21*		2.35*
				(6.28)	(3.81)	(2.20)
	j/j_∞	2.87	2.73	2.47	2.01	
		3.04*		2.53*		1.64*
				(2.11)	(1.85)	(1.54)
Change by rotation	f/f_B	−5%	−14%	−23% (+7%)	−21% (+17%)	+13% (+54%)
	j/j_∞	−4%	−11%	−20% (+1%)	−13% (+12%)	+25% (+45%)
Case B ($Re_m \fallingdotseq 3000$)						
$Ro_m = 0$ ($Ro_* = 0$)	f/f_B	13.41	–	9.38	–	1.91*
	j/j_∞	3.15	–	3.09	–	1.33*
$Ro_m \fallingdotseq 0.4$	f/f_B	13.12	–	7.25	–	3.01*
	j/j_∞	3.13	–	2.56	–	2.27*
Change by rotation	f/f_B	−2%	–	−23%	–	+58%
	j/j_∞	−1%	–	−17%	–	+71%

4. Conclusions

From the LES results of the turbulent heat transfer in a rectangular duct with the in-line angled-rib arrangement with and without rotation, the following conclusions were drawn.

In the 60° angled rib stationary case, the high heat transfer areas at the midpoint between the ribs and in front of the rib were shifted to the left wall due to the angled-rib induced secondary flow. For small aspect ratio (less than 1.0) with the wider rib-roughened surface, the wall-averaged heat transfer coefficient on the smooth left wall becomes higher than that on the smooth right wall; on the other hand, for large aspect ratio (greater than or equal to 1.0), the wall-averaged heat transfer coefficients on the right and left walls almost coincide. For small aspect ratio of the stationary case, the dissimilarity between the streamwise velocity and temperature profiles was observed. When the duct rotates, the dissimilarity was observed in all aspect ratio cases. The effect of the rotation in the 60° rib-roughened duct induced the larger spatial variation in the local heat transfer, and the heat transfer was increased and decreased on the pressure and suction sides, respectively; this tendency was similar to the results of the smooth duct and the 90° rib-roughened duct. However, the duct-averaged values (f and j factors) of the 60° rib case decreased by the effect of the rotation except the result for the aspect ratio of 4.0. It can be said that the flow field due to the Coriolis and angled-rib induced secondary flows was less effective in the heat transfer enhancement than that due to the angled ribs alone in the stationary condition for the aspect ratio less than or equal to 2.0.

References

[1] B. Lakshminarayana, Fluid Dynamics and Heat Transfer of Turbomach, John Wiley & Sons, New York, 1996, pp. 597–721 (Chapter 7).

[2] S. Mochizuki, A. Murata, M. Fukunaga, Effects of rib arrangements on pressure drop and heat transfer in a rib-roughened channel with a sharp 180° turn, Trans. ASME, J. Turbomach. 119 (1997) 610–616.

[3] S. Mochizuki, M. Beier, A. Murata, T. Okamura, Y. Hashidate, Detailed measurement of convective heat transfer in rotating two-pass rib-roughened coolant channels, ASME Paper, 96-TA-6, 1996.

[4] A. Murata, S. Mochizuki, T. Takahashi, Local heat transfer measurements of an orthogonally rotating square duct with angled rib turbulators, Int. J. Heat Mass Transfer 42 (1999) 3047–3056.

[5] P.R. Chandra, J.C. Han, S.C. Lau, Effect of rib angle on local heat/mass transfer distribution in a two-pass rib-roughened channel, Trans. ASME, J. Heat Transfer 110 (1988) 233–241.

[6] M. Hirota, H. Fujita, H. Yokosawa, T. Nakayama, T. Tanaka, Developing heat/mass transfer in low-aspect-ratio rectangular channels with ribbed walls, in: Heat Transfer 1998, Proceedings of 11th International Heat Transfer Conference, vol. 5, Taylor & Francis, 1998, pp. 363–368.

[7] G. Rau, M. Cakan, D. Moeller, T. Arts, The effect of periodic ribs on the local aerodynamic and heat transfer performance of a straight cooling channel, ASME Paper, 96-GT-541, 1996.

[8] J.W. Baughn, X. Yan, Local heat transfer measurements in square ducts with transverse ribs, Enhanced Heat Transfer ASME HTD-Vol. 202 (1992) 1–7.

[9] S.V. Ekkad, J.C. Han, Detailed heat transfer distributions in two-pass square channels with rib turbulators, Int. J. Heat Mass Transfer 40 (11) (1997) 2525–2537.

[10] C. Prakash, R. Zerkle, Prediction of turbulent flow and heat transfer in a ribbed rectangular duct with and without rotation, Trans. ASME, J. Turbomach. 117 (1995) 255–264.

[11] M.A. Stephens, T.I.-P. Shih, K.C. Civinskas, Effects of inclined rounded ribs on flow and heat transfer in a square duct, AIAA Paper, 95-2115, 1995.

[12] B. Banhoff, U. Tomm, B.V. Johnson, Heat transfer predictions for U-shaped coolant channels with skewed ribs and with smooth walls, ASME Paper, 96-TA-7, 1996.

[13] B.E. Launder, D.P. Tselepidakis, B.A. Younis, A second-moment closure study of rotating channel flow, J. Fluid Mech. 183 (1987) 63–75.

[14] A. Huser, S. Biringen, Direct numerical simulation of turbulent flow in a square duct, J. Fluid Mech. 257 (1993) 65–95.

[15] S. Gavrilakis, Numerical simulation of low Reynolds number turbulent flow through a straight square duct, J. Fluid Mech. 244 (1992) 101–129.

[16] R.K. Madabhushi, S.P. Vanka, Large eddy simulation of turbulence-driven secondary flow in a square duct, Phys. Fluids A 3 (11) (1991) 2734–2745.

[17] T. Kajishima, Y. Miyake, T. Nishimoto, Large eddy simulation of turbulent flow in a square duct, Trans. JSME (B) 57 (540) (1991) 2530–2537 (in Japanese).

[18] A. Murata, S. Mochizuki, Large eddy simulation with a dynamic subgrid-scale model of turbulent heat transfer in an orthogonally rotating smooth square duct, Int. J. Transport Phenom. 2 (2000) 27–41.

[19] A. Murata, S. Mochizuki, Effect of cross-sectional aspect ratio on turbulent heat transfer in an orthogonally rotating rectangular smooth duct, Int. J. Heat Mass Transfer 42 (1999) 3803–3814.

[20] A. Murata, S. Mochizuki, Large eddy simulation applied to internal forced-convection cooling of gas-turbine blades, in: Heat Transfer 1998, Proceedings of 11th International Heat Transfer Conference, vol. 6, Taylor & Francis, 1998, pp. 565–570.

[21] A. Murata, S. Mochizuki, Large eddy simulation with a dynamic subgrid-scale model of turbulent heat transfer in an orthogonally rotating rectangular duct with transverse rib turbulators, Int. J. Heat Mass Transfer 43 (2000) 1243–1259.

[22] A. Murata, S. Mochizuki, Large eddy simulation of turbulent heat transfer in an orthogonally rotating square

duct with angled rib turbulators, Trans. ASME, J. Heat Transfer 123 (2001) 858–867.
[23] A. Murata, S. Mochizuki, Comparison between laminar and turbulent heat transfer in a stationary square duct with transverse or angled rib turbulators, Int. J. Heat Mass Transfer 44 (2001) 1127–1141.
[24] M.E. Taslim, S.D. Spring, Effect of turbulator profile and spacing on heat transfer and friction in a channel, J. Thermophys. Heat Transfer 8 (3) (1994) 555–562.
[25] G.J. Korotky, M.E. Taslim, Rib heat transfer coefficient measurements in a rib-roughened square passage, ASME Paper, 96-GT-356, 1996.
[26] J.C. Han, J.S. Park, C.K. Lei, Heat transfer enhancement in channels with turbulence promoters, Trans. ASME, J. Eng. Gas Turb. Power 107 (1985) 628–635.
[27] S.V. Patankar, C.H. Liu, E.M. Sparrow, Fully developed flow and heat transfer in ducts having streamwise-periodic variations of cross-sectional area, Trans. ASME, J. Heat Transfer 99 (1977) 180–186.
[28] T. Kajishima, T. Ohta, K. Okazaki, Y. Miyake, High-order finite-difference method for incompressible flows using collocated grid system, JSME Int. J. Series B 41 (4) (1998) 830–839.
[29] M. Germano, U. Piomelli, P. Moin, W.H. Cabot, A dynamic subgrid-scale eddy viscosity model, Phys. Fluids A 3 (7) (1991) 1760–1765.
[30] D.K. Lilly, A proposed modification of the germano subgrid-scale closure method, Phys. Fluids A 4 (3) (1992) 633–635.
[31] C. Meneveau, T.S. Lund, W.H. Cabot, A Lagrangian dynamic subgrid-scale model of turbulence, J. Fluid Mech. 319 (1996) 353–385.
[32] P. Moin, K. Squires, W. Cabot, S. Lee, A dynamic subgrid-scale model for compressible turbulence and scalar transport, Phys. Fluids A 3 (11) (1991) 2746–2757.
[33] F.H. Harlow, J.E. Welch, Numerical calculation of time-dependent viscous incompressible flow of fluid with free surface, Phys. Fluids 8 (12) (1965) 2182–2189.
[34] J. Kim, P. Moin, Application of a fractional-step method to incompressible Navier–Stokes equations, J. Comput. Phys. 59 (1985) 308–323.
[35] Y. Zang, R.L. Street, J.R. Koseff, A non-staggered grid, fractional step method for time-dependent incompressible Navier–Stokes equations in curvilinear coordinates, J. Comput. Phys. 114 (1994) 18–33.
[36] W.M. Kays, M.E. Crawford, Convective Heat and Mass Transfer, third ed., McGraw-Hill, New York, 1993, p. 316.